IEEE Access
Multidisciplinary | Rapid Review | Open Access Journal

Received 13 July 2022, accepted 3 August 2022, date of publication 16 August 2022, date of current version 22 August 2022.

Digital Object Identifier 10.1109/ACCESS.2022.3198991

RESEARCH ARTICLE

Eliminating the Resonance Interference for an Inductive Speed Sensor Subjected to an Early-Time HEMP Field

HAITAO WANG[1], DONG ZHOU[1], MINXIANG WEI[2], AND WEIWEI QIAN[3]
[1]Army Engineering University of PLA, Nanjing 210007, China
[2]Nanjing University of Aeronautics and Astronautics, Nanjing 210016, China
[3]Nanjing University of Information Sciences and Technology, Nanjing 210044, China

Corresponding author: Dong Zhou (2396765419@qq.com)

ABSTRACT In the present study, the mechanism of electromagnetic resonance interference on an inductive speed sensor is investigated. To this end, a second-order equivalent resonance model is established based on the lumped parameter of the speed sensor. Then the effects of different parameters on the interference signal are analyzed. The effect of terminal loads and filter capacitances are simulated in the CST software and the obtained results for the resonance interference signal are analyzed. Moreover, an experiment is carried out and the oscillation of the voltage interference signal is produced by the speed sensor under the testing of early-time high altitude nuclear electromagnetic pulse (HEMP) field. The GTEM cell is used to produce the plane wave for the experiment. Finally, the advantages and disadvantages of different resonance elimination methods are analyzed, and the method is proposed to eliminate the oscillation of the voltage interference signal.

INDEX TERMS Equivalent model, elimination methods, HEMP, resonance interference, speed sensor.

I. INTRODUCTION

A high-altitude electromagnetic pulse (HEMP) is generated by the high-altitude nuclear explosion. Studies show that the rich frequency spectrum of early-time HEMP is a serious threat to electronic control systems. Accordingly, this issue has attracted great interests and concerns in past few decades [1], [2].

With the rapid development of electric vehicles, HEMP interference to cars draws lots of attention in recent years. Electromagnetic susceptibility of car engine and parts to narrowband microwaves in the 1–2.5 GHz band is reported in [3]. The wideband pulse interference to automotive electrical components to in the range of 400 MHz–2.8 GHz is tested [4]. The influence of high electromagnetic interference generated by high-voltage electrical components is also studied [5]. Intentional electromagnetic interference experiments were conducted to characterize the vulnerability of a vehicle [6].

The associate editor coordinating the review of this manuscript and approving it for publication was Wuliang Yin.

While, the majority of investigations in this area are focused on the coupling of wires, including the shield wire and twisted pairs, through numerical simulations and experiments [7], [8], [9]. The shielding effectiveness of connectors and conductive cavities have been studied in detail [10], [11], [12]. The main concerns of these works is the breakdown of the PCB board in the controller [13], [14].

With the continuous development of intellectualization, various sensors are used in automotive controlled systems so that the HEMP effect on the system has become more important. In this regard, Zhou *et al.* [15] conducted experiments and numerical simulations to study the HEMP effects on the electronic control system of an engine and verified the interference characteristics of HEMP on the control system. Recently, the interior electromagnetic field distribution of the car subjected to HEMP radiation field has been studied [16]. Meanwhile, Yang *et al.* [17] applied a HEMP simulator to investigate the HEMP effects on the electronic control system of an engine. Accordingly, it was found that the HEMP has a significant impact on the engine control system. Zhou *et al.* [18] carried out numerical simulations

and experiments to study the HEMP effects on the engine speed sensor and showed that the sensor is susceptible to HEMP. However, permanent damage was not detected in the test. Aiello *et al.* [19] conducted experiments and studied the electromagnetic susceptibility of Hall effect sensors. Tang *et al.* [20] studied the influence of overvoltage and electromagnetic radiation generated by the PCA on the signal of speed sensors, and revealed the influence of the radiation on the signal. At the same time, the software interference elimination method is also very important. Qiao *et al.* [21] used the stochastic resonance for realizing mechanical fault detection. Sun and Chang [22] applied wavelet packet transform to structural damage assessment. Considering software reliability, hardware protection is selected in this paper. Reviewing the literature indicates that despite the importance of inductive speed sensors, only a few studies have focused on the electro-magnetic interference mechanism of these components. In the present study, it is intended to investigate the interference mechanism of inductive speed sensors subjected to the HEMP. To this end, the oscillating interference mechanism of the speed sensor will be analyzed and numerical simulation will be carried out on the established model.

The contents of this article are organized as follows. Section II introduces the speed acquisition system. In Section III, the gigahertz transverse electromagnetic wave transmission cell (GTEM) is used to produce the plane wave for the experiment. Then the oscillation interference of the voltage signal is proved by the speed sensor subjected to the early-time HEMP field. In Section IV, the effect of terminal loads and filter capacitances are analyzed numerically through an equivalent resonance model. In Section V, the second-order equivalent resonance model is established to analyze the resonance interference mechanism of the inductive speed sensor. Finally, the advantages and disadvantages of different resonance elimination methods are analyzed.

II. INTRODUCTION OF SPEED ACQUISITION SYSTEM

Generally, a speed acquisition system consists of an inductive speed sensor and a signal proceeding circuit. Figure 1 reveals that the speed sensor is installed near the top of the rotating tooth wheel by a support frame, consisting of a permanent magnet, a core and a coil. It is worth noting that a permanent magnet is applied to provide a constant magnetic field for the speed sensor. When the wheel rotates, a time-varying magnetic flux is produced in the core of the speed sensor. Then the speed sensor produces the speed signal based on the variation of the magnetic flux. This signal depends on the rotating speed of the wheel, the variation rate of the magnetic flux, the wheel diameter and the number of teeth on the wheel [23]. Figure 2 shows the installed speed sensor on the engine body. When the engine works, the speed sensor sends an alternating signal corresponding to the variations of the magnetic flux. Accordingly, the wheel speed can be converted to the frequency signal. Then a specified chip (MAX9926, Maxim Company, USA) is used to transform the sinusoidal signal into the typical rotary encoder signal.

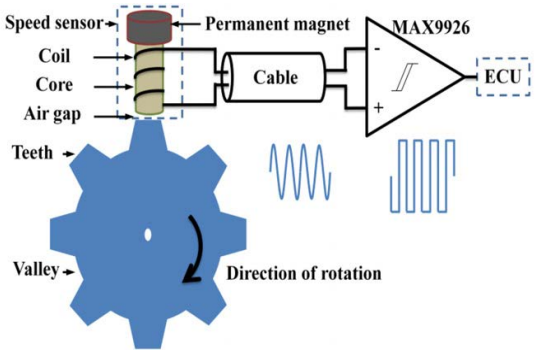

FIGURE 1. Schematic diagram of the speed acquisition system.

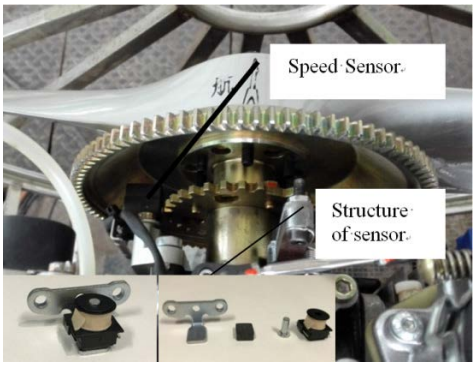

FIGURE 2. Configuration of the speed sensor.

III. RESONANCE EXPERIMENT VALIDATION

A. HEMP WAVEFORM

In order to describe the electromagnetic pulse, a double exponential plane wave [24] can be employed as an excitation source in the numerical simulation. This can be mathematically expressed in the form below:

$$E(t) = kE_p\left(e^{-\alpha t} - e^{-\beta t}\right). \tag{1}$$

where E_p is the peak excitation value, and $k = 1/(e^{-\alpha tp} - e^{-\beta tp})$ is a modifying factor, and t_p is the rising time of electric field. Moreover, α and β are characteristic parameters satisfying the condition $\beta > \alpha > 0, \forall t \geq 0$. Figure 3 presents the characteristic curves of HEMP.

B. EXPERIMENT VALIDATION

In this section, it is intended to prove that resonance occurs in the speed sensor exposed to the radiant electromagnetic fields. Considering the small size of the speed sensor, a GTEM cell is applied to produce an electromagnetic field during the experiment. It should be indicated that the GTEM cell has a low leakage so that it has a low interference on external instruments and surrounding operators. Table 1 presents the equipment list in the performed experiment.

A double exponential pulse source is used to excite the GTEM cell. Moreover, a differentiator is used to monitor the signal characteristics of the pulse source. A calibrated electric field probe is installed in the GTEM cell to measure the

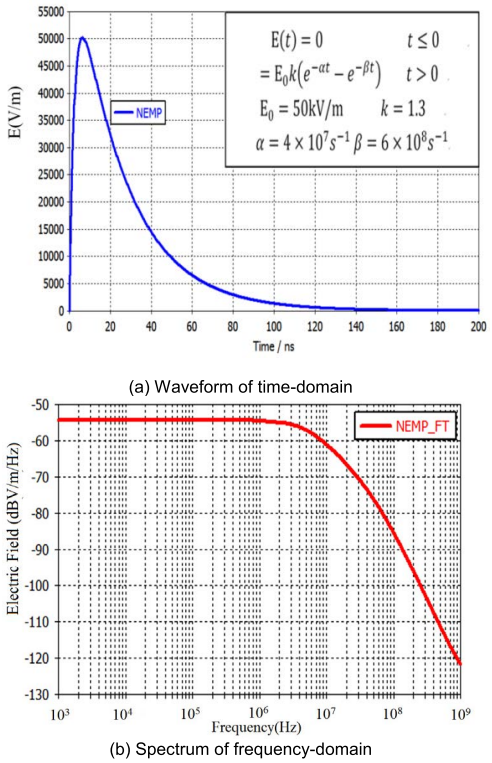

FIGURE 3. Characteristic curves of nuclear electromagnetic pulses.

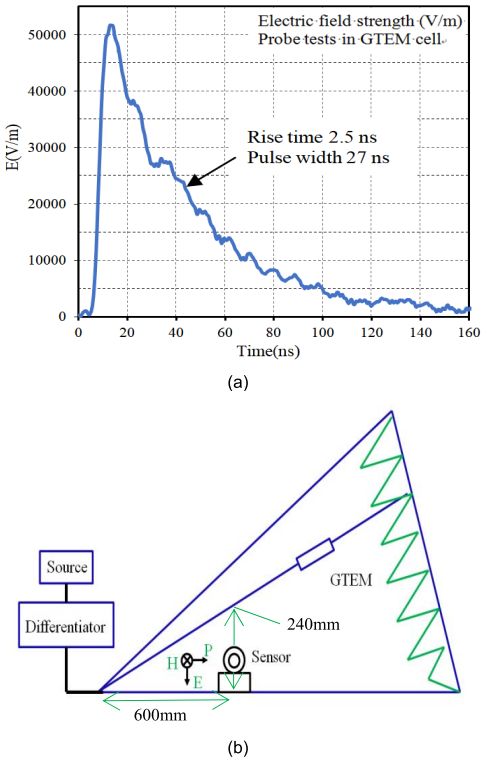

FIGURE 4. (a) Measured electric field waveform of the GTEM cell, (b) Schematic layout of the speed sensor in the GTEM cell.

TABLE 1. Test equipment list.

Equipment	Parameter	Unit
Pulse Source	Peak voltage 30 Rise time 2 Pulse width 25	kV ns ns
GTEM Cell	Max field amplitude≥50 SWR≤1.4	kV/m
Electric field probe	Max field amplitude≥50	kV/m
Voltage Probe	Tektronix P6015A	
Oscilloscope	Tektronix TBS1104	
Signal generator	Tektronix 2012B	

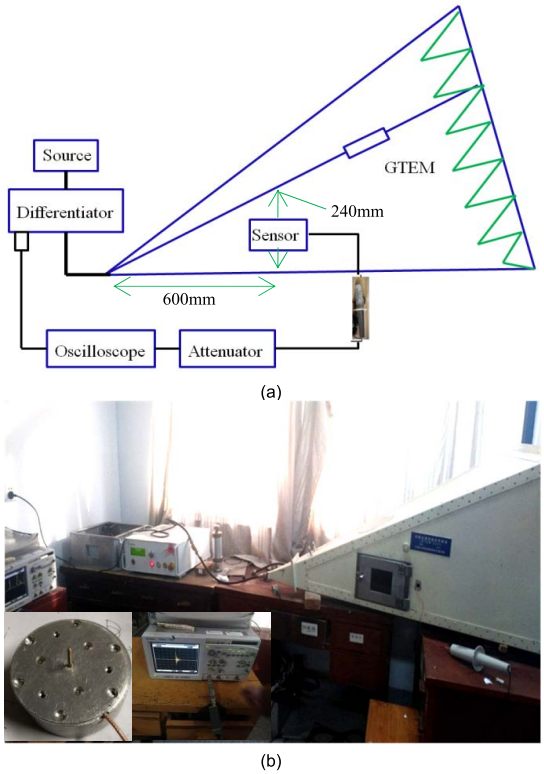

FIGURE 5. (a) Schematic coupling experiment diagram, (b) Configuration of the coupling experiment.

electric field strength. Due to the small volume of the speed sensor, the GTEM cell provides a sufficient enough effective area for the test. Figure 4(a) presents the measured electric field waveform inside the GTEM cell.

In the experiment, the speed sensor is located in the effective area at an appropriate distance from the GTEM cell. Figure 4(b) indicates that the coil axis is parallel to the direction of the magnetic field, which is used to increase the field coupling. The terminal coupling signal of the speed sensor is recorded by a voltage probe (P6015A, Tektronix, USA). The total attenuation coefficient is 3162, which includes a 1000 times attenuation of the voltage probe and a 10 dB attenuator connecting to the oscilloscope. Figure 5 shows the test scenario of the experiment.

Figure 6(a) presents the resonance period of the speed sensor interference. Moreover, the resonance duration is shown

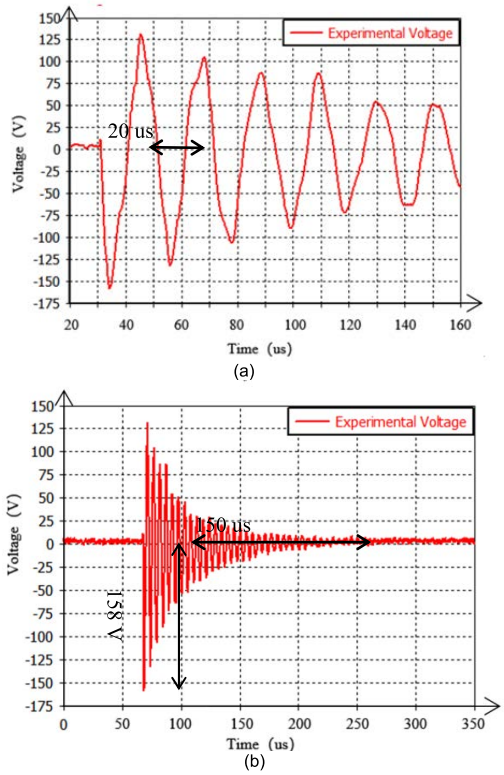

FIGURE 6. Voltage waveform diagram.

in Figure 6(b). It is found that the resonance period of the interference signal and the max amplitude are about 20 us and 158 V, respectively. The total duration of the resonance phenomenon is about 150 us so that it can be simply captured by the controller. Then the electromagnetic resonance interference is produced from the inductive speed sensor.

IV. FULL-WAVE SIMULATING THE SPEED SENSOR RESONANCE

In the previous section, the speed sensor resonance was proved by testing the electromagnetic field experiment. Then the influence of the terminal impedance and the filter capacitance is analyzed to study the speed sensor resonance. To this end, the full-wave simulation method is applied in the present study.

In order to obtain the influence of parameters on the speed sensor resonance, CST Microwave Studio is used to simulate the electromagnetic coupling effect of the speed sensor subjected to the HEMP. Figure 1 indicates that the frequency spectrum characteristics of HEMP (E_1) up to 1 GHz can be achieved to cover the main power. Then the maximum frequency is set to 1 GHz to meet simulation requirements. Moreover, boundaries in all directions are assumed ''open'' boundaries in the simulation. The polarization and propagation direction of the plane wave is selected as shown in Figure 8. The terminal load is set as the lumped element. In all simulations, the hexahedral TLM method is applied to simulate the resonance effects on the speed sensor. The coils of the speed sensor consist of several thousand wire turns, which is hard to model in the simulation. Considering the skin effect and proximity effect of the wire exposed to high-frequency testing fields, a simplified model of the inductive speed sensor is established, which is shown in Figure 7 [25]. In the simplified model, 10 turns of wire are considered in each layer of the coil.

In order to simulate the air gap between the speed sensor and the wheel, a closed state model is built. Figure 7 indicates that a circular core is applied to simulate the low-resistance magnetic circuit consisting of the sensor and the support frame. The air gap, cutting from a circular core, is used to present the small space between the core and wheel. Parameters of the simplified model are listed in Table 2.

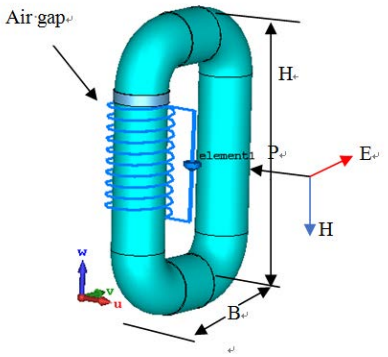

FIGURE 7. The simplified 3D model of the studied inductive speed sensor.

TABLE 2. Parameters of simplified model.

Parameter name	Value	Unit
Coil Turns	10	turns
Coil Diameter	8	mm
Coil Pitch	1	mm
Core Diameter	7	mm
Air Gap	2	mm
B	17	mm
H	27	mm
Terminal Resistance	10	kΩ

Accordingly, it is found that the resonance can be eliminated by reducing the terminal load resistance or increasing the filter capacitance. In this section, the influences of terminal load resistance and filter capacitance on the output voltage resonance are studied. In engineering applications, the speed acquisition system is connected to a high-impedance chip to reduce the input energy loss. Since the parallel resistance can reduce the terminal resistance, different resistance values are considered in simulations. In this regard, terminal loads of 1 MΩ, 10 kΩ and 50 Ω are used in simulations. Figure 8 presents the obtained results. Moreover, Figure 9 shows the influence of the filter capacitance on the resonance output voltage. In this regard, four filter capacitance values,

including 0 pF, 10 pF, 100 pF and 0.01 μF, are considered in simulations.

Figure 8 indicates that the resonance can be eliminated by reducing the load resistance. However, the small load resistance is connected to the end load in a parallel mode. It is observed that the resonance disappears with a parallel resistance of 50 Ω. On the other hand, when the parallel resistance exceeds 100 kΩ, resonance occurs. Meanwhile, as the resistance drops in the time domain, the corresponding coupling voltage amplitude and the amplitude of the resonance frequency decrease. However, Figure 8(a) demonstrates that the resonance frequency almost remains constant in the frequency domain. The disadvantage of this issue will be analyzed in the next section.

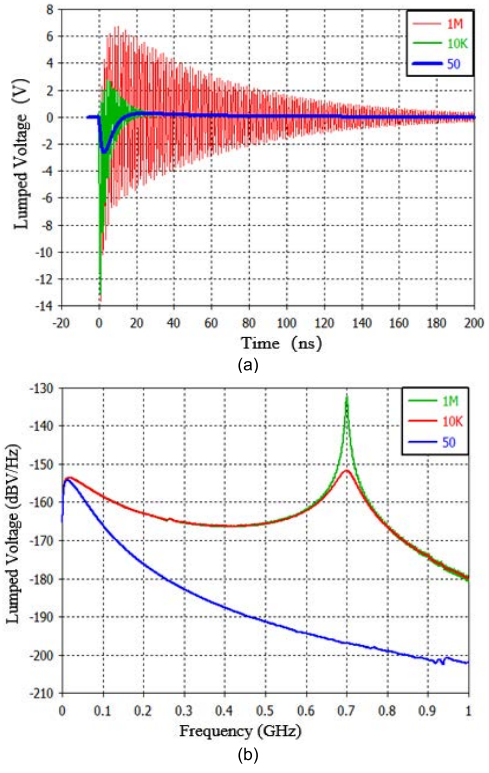

FIGURE 8. (a) Voltage-time waveforms for different loads. (b) Voltage-frequency waveforms for different loads.

Figure 9 shows that the resonance can also be eliminated by applying the filter capacitance. Moreover, the coupling voltage amplitude decreases as the filter capacitance in the time domain increases. However, the difference from the resistance matching is that the resonance frequency reduces with the increasing of the filter capacitance in the frequency domain. When the filter capacitance reaches 0.1 μF, the resonance disappears. Then further decrease of the resonance frequency results in the cutoff of the high-speed signal. This issue will be analyzed in the next section. Although the parallel capacitance value of 10 pF does not affect the speed signal transmission, it also cannot resolve the resonance problem.

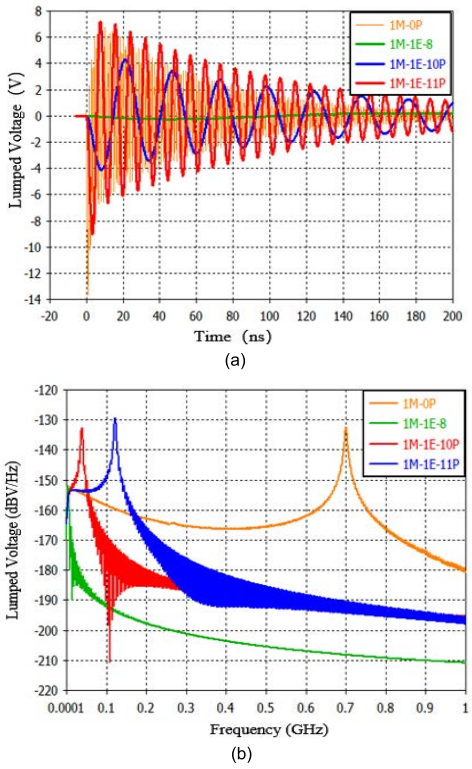

FIGURE 9. (a) Voltage-time waveforms for different loads. (b) Voltage-frequency waveforms for different loads.

V. MECHANISM ANALYSIS OF THE SECOND-ORDER EQUIVALENT MODEL

A. ANALYSIS OF THE RESONANCE ELIMINATION

To deeply analyze the interference mechanism, a second-order equivalent resonance model is established based on the lumped parameter and normal loads in an inductive speed sensor. Figure 10 shows the established model. In the model, the electric and magnetic field components in the plane wave are transformed into equivalent magnetic flux using Maxwell equations. In this way, the model can be established only by the equivalent inductance (L_c), equivalent resistance (R_c), and coil equivalent lumped capacitance (C_c) of the inductive speed sensor. Meanwhile, the capacitive filter (C_P) and load resistance (R_t) are also included in the model. Main parameters of the model are the lumped parameters and load parameters of the inductive speed sensor.

In the presented schematic circuit, R_c, L_c and $V_{rc}(t)$ are the resistance, inductance and instantaneous inductive voltage of the coil equivalent resistance in the speed sensor, respectively. Moreover, C_c and C_P denote the coil equivalent lumped capacitance of the inductive speed sensor and the capacitive filter, respectively. R_t is the equivalent resistance of load and $V_0(t)$ is the output voltage of the inductive speed sensor. The E, H and P denote the electric field component, magnetic field component and propagation direction for EMP plane wave.

When a plane wave interacts with the inductive speed sensor, the magnetic field component is perpendicular to the coil

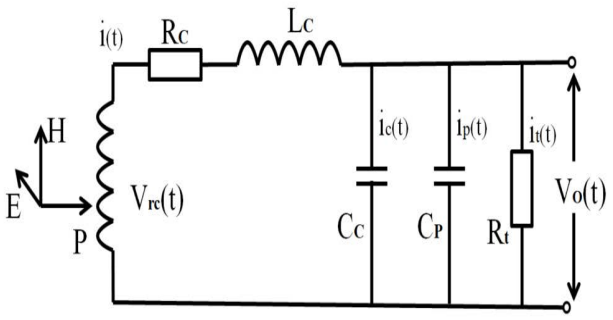

FIGURE 10. Second-order equivalent resonance mode of speed sensor.

plane so that the maximum coupling voltage can be obtained. The coil equivalent inductive voltage of the inductive speed sensor can be calculated through the following expression:

$$\mu\mu V_{rc}(t) = -_0 inA\frac{dH}{dt} \tag{2}$$

where μ_0 and μ_i denote the relative permeability of air and core, respectively. Furthermore, n is the number of turns of the coil, and A is the area of each turn. The term dH/dt reflects the change rate of equivalent magnetic flux.

The relation between $V_0(t)$ and $V_{rc}(t)$ in Figure 10 can be obtained from Kirchhoff's law in the form below:

$$\begin{cases} V_{rc}(t) = L_c\dfrac{di(t)}{dt} + R_c i(t) + V_0(t) \\ i(t) = C\dfrac{dV_0(t)}{dt} + \dfrac{V_0(t)}{R_t} = i_c(t) + i_{Rt}(t) \end{cases} \tag{3}$$

This equation can be simplified based on the following assumptions:

$$i_c(t) = C\frac{dV_0(t)}{dt}, \quad i_{Rt}(t) = \frac{V_0(t)}{R_t}, \; C = C_c + C_p \tag{4}$$

where C is the terminal equivalent capacitance of the speed sensor. C_c is equivalent lumped capacitance, and C_P is capacitive filter Moreover, $i_c(t)$ is denotes the current passing the load C_c. $i_{Rt}(t)$ is denotes the current passing the load R_t. $i(t)$ is denotes the current passing the load R_c.

Accordingly, equation (3) can be rewritten in the form below:

$$\begin{aligned} V_{rc}(t) &= L_c C\frac{d^2V_0(t)}{dt^2} + L_c\frac{1}{R_t}\cdot\frac{dV_0(t)}{dt} + R_c C\frac{dV_0(t)}{dt} \\ &\quad + R_c\frac{V_0(t)}{R_t} + V_0(t) \\ &= L_c C\frac{d^2V_0(t)}{dt^2} + \left(\frac{L_c}{R_t} + R_c C\right)\frac{dV_0(t)}{dt} \\ &\quad + \left(\frac{R_c}{R_t} + 1\right)V_0(t) \end{aligned} \tag{5}$$

Introducing equation (2) into equation (5) yields the following expression:

$$\begin{aligned} -M\frac{dH}{dt} &= L_c C\frac{d^2V_0(t)}{dt^2} + \left(\frac{L_c}{R_t} + R_c C\right)\frac{dV_0(t)}{dt} \\ &\quad + \left(\frac{R_c}{R_t} + 1\right)V_0(t) \end{aligned} \tag{6}$$

where $M = \mu_0\mu_i nA$, M is the mutual inductance of the coil. This equation describes the correlation between the time derivative of the magnetic field and the output voltage of the speed sensor. Applying the Laplace transformation, equation (6) converts to equation (7). It is worth noting that the Laplace transformation converts the time domain to the S-domain. As a result, the correlation between $V_0(s)$ and $H(s)$ can be described by sensor parameters, load parameters and filter parameters.

$$\begin{aligned} -MsH(s) &= L_c Cs^2 V_0(s) + \left(\frac{L_c}{R_t} + R_c C\right)sV_0(s) \\ &\quad + \left(\frac{R_c}{R_t} + 1\right)V_0(s) \end{aligned} \tag{7}$$

where M is the mutual inductance of the coil. s is the Laplace transformation parameter. V_0(s) and H(s) are the output voltage, magnetic field intensity after Laplace transformation.

Similarly, the correlation between $V_0(s)$ and H can be expressed in the form below:

$$\begin{aligned} V_0(s) &= \frac{-MsH(s)}{L_c Cs^2 + \left(\frac{L_c}{R_t} + R_c C\right)sV_0(s) + \left(\frac{R_c}{R_t} + 1\right)} \\ &= \frac{-M\frac{1}{L_c C}}{s^2 + \frac{1}{L_c C}\left(\frac{L_c}{R_t} + R_c C\right)s + \frac{1}{L_c C}\left(\frac{R_c}{R_t} + 1\right)}\cdot sH \end{aligned} \tag{8}$$

where $M/L_c C$ is a constant term. For the second-order transfer function, the resonance of the speed sensor can be described by lumped parameters. In this regard, the resonance frequency and the damping ratio are two important parameters. It is worth noting that one of the key points of the present study is resonance elimination. Then, the damping ratio is the dominant parameter when it is compared with the resonance frequency. It is assumed that the denominator of equation (8) is zero. Accordingly, the second-order transfer function between coupling voltage and magnetic field rate can be expressed in the form below:

$$s^2 + \frac{1}{L_c C}\left(\frac{L_c}{R_t} + R_c C\right)s + \frac{1}{L_c C}\left(\frac{R_c}{R_t} + 1\right) = 0 \tag{9}$$

Then:

$$\begin{cases} 2\xi\omega_n = \dfrac{1}{L_c C}\left(\dfrac{L_c}{R_t} + R_c C\right) \\ \omega_n^2 = \dfrac{1}{L_c C}\left(\dfrac{R_c}{R_t} + 1\right) \end{cases} \tag{10}$$

where $|\omega_n|$ is the resonance frequency of output voltage V_0. And ξ is the damping factor of the second-order transfer function. Then the damping factor can be described by lumped parameters in the form below:

$$4\xi^2 = \frac{L_c}{R_t(R_c + R_t)}\frac{1}{C} + \frac{R_t^2 R_C^2}{L_c R_t(R_c + R_t)}C + \frac{2R_t R_c}{R_t(R_t + R_c)} \tag{11}$$

Analyzing the derived second-order transfer function results in the resonance of output voltage (if any). Whether the resonance occurs, it can be mainly determined by the damping ratio. When the damping coefficient exceeds 1.0, then the resonance does not occur in the output voltage of the speed sensor. In contrast, the output voltage resonates for the damping coefficient less than 1.0. In this case, the resonance frequency is shown in equation (10).

B. ANALYSIS OF THE RESONANCE ELIMINATION

The second-order equivalent resonance model was used to analyze the output voltage resonance of the speed sensor. The obtained results from the experiment and numerical simulations demonstrate the occurrence of the resonance phenomenon in the output voltage. Analyzing the established model indicates that the resonance in the output voltage mainly originates from the low-damping feature of the speed sensor system. The damping ratio is an important parameter to describe the damping characteristics. The affecting parameters on the damping ratio are presented in Equation (10). However, not all parameters can be adjusted to reduce the damping ratio. In particular, parameters corresponding to the inherent characteristics of the sensor are adjusted only once in the factory, while the load resistance (R_tR$_t$) and filter capacitor (C_pC$_p$) can be adjusted in the experiment. Then common resonance suppression methods are discussed as follow:

1) ELIMINATING THE DISTRIBUTED CAPACITANCE

When the speed sensor is designed to eliminate the distributed capacitance (Cc), the resonance problem can be resolved. This is because the resonance originates from the distributed capacitance in the established model. However, this concept has high requirements on the material and structure of the speed sensor. Consequently, this scheme is not feasible.

2) TERMINAL IMPEDANCE MATCHING

Solution of equation (9) for the damping ratio can be expressed in the form below:

$$2\xi = \sqrt{\frac{1}{L_c C}}\left(\frac{L_c}{R_t} + R_c C\right)\sqrt{\frac{R_c}{R_c + R_t}} \tag{12}$$

This equation shows that the damping ratio increases with the decrease of the load resistance. Accordingly, the method of decreasing load resistance can be applied to eliminate the resonance. Therefore, high-impedance chips are considered for the input resistance to reduce the input current. In this regard, Shunt resistors are used to reduce the input load impedance at point A. However, this method also reduces the voltage amplitude at point B. Although this method resolves the resonance problem of the speed sensor, the smaller amplitude cannot drive the chip so that the entire system does not work properly.

3) CAPACITIVE FILTERING METHOD

Parallel capacitance can be applied to resolve the resonance problem in the terminal of the speed sensor. In this method, a high capacitance is required, which limits the top frequency of the signal transmission. Then the parallel capacitance satisfies the analog signal transmission of the speed sensor. In this approach, the calculation of the capacitance range for the capacitive filter is of significant importance.

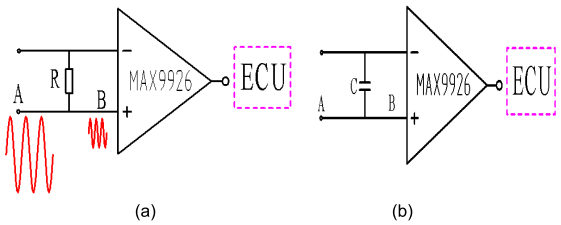

FIGURE 11. Matching circuit of chip front end.

In this approach, the capacitance value should satisfy the non-resonance condition (e.g. $\xi \geq 1$). Supposing that the damping ratio is $\xi = 1$, equation (10) transforms into the quadratic function of the capacitance in the form below:

$$C^2 + \frac{2R_t R_c L_c - 4R_t\left(R_c + R_t\right)L_c}{R_t^2 R_C^2} C + \frac{L_c^2}{R_t^2 R_C^2} = 0 \tag{13}$$

Solving this equation results in capacitance as the following:

$$C = \frac{L_c}{R_c}\left[\left(\frac{1}{R_t} + \frac{2}{R_c}\right) \mp 2 \cdot \sqrt{\left(\frac{1}{R_c}\right)^2 + \frac{1}{R_t R_c}}\right] \tag{14}$$

The result of the capacitance is so complex that it cannot be applied in engineering applications. Moreover, it is a challenge to obtain the capacitance through this equation. Accordingly, it is necessary to simplify this expression. It is worth noting that the chip is considered as the speed system load and the load equivalent resistance R_t is much more than the sensor equivalent resistance R_c. Generally, $R_t > 1M\Omega$ while $R_c < 10\,\Omega$. Consequently, the following approximation is made:

$$lim\,\frac{1}{R_t} \to 0 \tag{15}$$

Then equation (13) can be simplified into equation (14).

$$C = \frac{4L_c}{R_c^2} \tag{16}$$

According to the opening characteristics of the parabola, the damping ratio increases as the capacitance value increases. The condition to ensure that the speed acquisition system does not resonate is $C \geq 4L_c/R_c^2$.

The comparisons of parallel resistance and capacitance are shown as Figure 12. Obviously, Figure 12 (a) shows that both methods can eliminate the resonance phenomenon in the output voltage. And parallel capacitance method has better results for high frequency suppression. Figure 12 (b) gives the

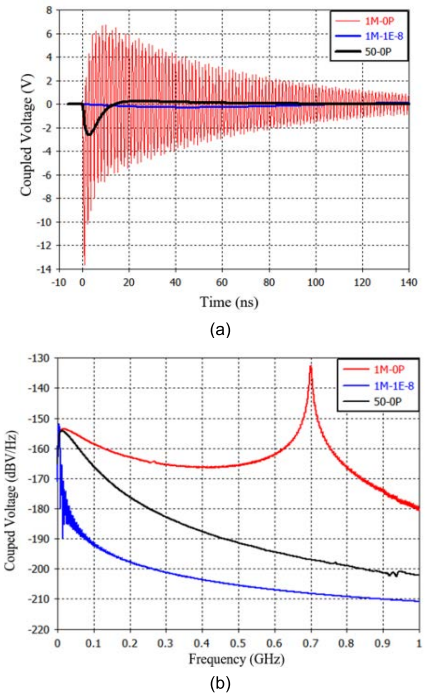

FIGURE 12. **(a) Voltage-time waveforms for different loads. (b) Voltage-frequency waveforms for different loads.**

suppression mechanism is reducing the resonant frequency and amplitude through the terminal load. The parallel capacitance line is lower than the parallel resistance line, which confirms the result that the parallel capacitance is more effective. Then, it reflects that the parallel resistance has wider work-frequency characteristic. This characteristic allows the speed sensor to work at a higher speed.

The speed sensor is an inductive sensor with a large inductance. Equation (14) indicates that the sensor needs a large parallel capacitance at the load side. This large capacitance prevents high-frequency analog signals from reaching the controller terminal and makes the speed system not work at high speeds, thereby reducing the measuring width of the sensor. In order to ensure the high-speed characteristics of the speed measurement system, the new method of parallel resistance was put forward to eliminate the resonance in the at high speed equipments. And the development of microcomputer technology makes the algorithm in real-time, which makes algorithm to eliminate resonance interference a great value in the future.

VI. CONCLUSION

In the present study, the resonance interference mechanism of the speed sensor subjected to the HEMP field is analyzed. To this end, the second-order equivalent model is established to analyze the effects of different parameters on the resonance of the inductive speed sensor. Then the GTEM cell is applied to conduct experiments and validate the simulated resonance interference. Based on the obtained results, the disadvantages of the parallel resistance and capacitance filter for eliminating the resonance are discussed. Meanwhile, the effects of parallel resistance and capacitance filtering for eliminating resonance have been simulated. Finally, a magnetic ring transformer is proposed to eliminate the resonance by increasing the damping ratio of the speed acquisition system. The present article is expected to provide a reference to reinforce the inductive speed sensor subjected to nuclear electromagnetic pulses.

ACKNOWLEDGMENT

The authors would like to thank all the reviewers who participated in the review and MJEditor (www.mjeditor.com) for its linguistic assistance during the preparation of this manuscript. It also includes Peng Li, Mingjie Sheng, and KYGYJQZL2205 for experiment support and checking this paper.

REFERENCES

[1] W. A. Radasky, "Generation of high-altitude electromagnetic pulse (HEMP)," in *Proc. IEEE Int. Symp. Electromagn. Compat.*, Aug. 2008, pp. 1–5.
[2] S. Mazzola, "MIL-STD-461: The basic military EMC specification and it's evolution over the years," in *Proc. IEEE Long Island Syst., Appl. Technol. Conf.*, May 2009, pp. 1–5.
[3] S. A. Mitilineos, V. Dedes, D. N. Clemente, N. Kevlishvili, S. Kuhlmann, S. P. Savaidis, N. Stathopoulos, Z. C. Ioannidis, C. Tsitouri, E. Papadogeorgos, N. G. Apergis, and M. Martinez-Vazquez, "Electromagnetic susceptibility of car engine and parts to narrowband microwaves in the 1–2.5 GHz band," *IEEE Trans. Electromagn. Compat.*, vol. 63, no. 5, pp. 1366–1375, Oct. 2021.
[4] T. Picon, T. Dubois, M. Klingler, and G. Duchamp, "Methodology to test automotive electrical components to wideband pulse interferences," *IEEE Trans. Electromagn. Compat.*, vol. 62, no. 5, pp. 1651–1660, Oct. 2020.
[5] J. Hu, X. Xu, D. Cao, and G. Liu, "Analysis and optimization of electromagnetic compatibility for electric vehicles," *IEEE Electromagn. Compat. Mag.*, vol. 8, no. 4, pp. 50–55, 4th Quart., 2019.
[6] Y. Zhong, W. Song, C. Kim, C. Park, and C. Hwang, "Efficient automotive simulation using reciprocity for intentional electromagnetic interference," in *Proc. IEEE Int. Symp. Electromagn. Compat., Signal Power Integrity (EMC SIPI)*, Jul. 2019, pp. 600–604.
[7] S. A. Pignari and G. Spadacini, "Plane-wave coupling to a twisted-wire pair above ground," *IEEE Trans. Electromagn. Compat.*, vol. 53, no. 2, pp. 508–523, Oct. 2010.
[8] Z. Liuhui, Z. Yinghui, S. Zheng, and S. Lihua, "Study on the measurement method for transfer impedance of multi-conductor shielded cable in time-domain," in *Proc. IEEE 11th Int. Conf. Electron. Meas. Instrum.*, Aug. 2013, pp. 664–667.
[9] X. Liu, F. Grassi, G. Spadacini, and S. A. Pignari, "Physically based modeling of hand-assembled wire bundles for accurate EMC prediction," *IEEE Trans. Electromagn. Compat.*, vol. 62, no. 3, pp. 914–922, Jun. 2019.
[10] E. B. Savage, W. A. Radasky, and R. Willliamson, "Time domain measurement of shielded cables with connectors," in *Proc. IEEE Int. Symp. Electromagn. Compat. (EMC)*, Jul. 2016, pp. 148–152.
[11] G. Zhang, T. Wei, J. Ding, and C. Guo, "The calculation and analysis of shielding efficiency," in *Proc. IEEE Int. Appl. Comput. Electromagn. Soc. Symp. (ACES)*, Aug. 2017, pp. 1–2.
[12] J. Xiao, Z. Song, J. Wang, and L. Wang, "Simulation analysis of electromagnetic shielding of electronic device chassis," in *Proc. 12th Int. Workshop Electromagn. Compat. Integr. Circuits (EMC Compo)*, Oct. 2019, pp. 91–93.
[13] M. Camp, H. Gerth, H. Garbe, and H. Haase, "Predicting the breakdown behavior of microcontrollers under EMP/UWB impact using a statistical analysis," *IEEE Trans. Electromagn. Compat.*, vol. 46, no. 3, pp. 368–379, Aug. 2004.
[14] C. Du, D. Xia, Q. Huang, C. Mao, Z. Cui, W. Fang, and X. Nie, "Research on electromagnetic susceptibility of electronic modules in component-level HEMP PCI test," *Energies*, vol. 15, no. 4, p. 1409, Feb. 2022.
[15] D. Zhou, M. Wei, L. Shi, J. Cao, and L. Su, "Experimental analysis of electromagnetic pulse effects on engine fuel electronic control system," *Int. J. Appl. Electromagn. Mech.*, vol. 65, no. 1, pp. 45–57, Jan. 2021.

[16] C. Jinliang, Z. Xiaohui, S. Xiaoying, and C. Jian, "Effects of Windows to the electromagnetic environment of a car radiated by high altitude electromagnetic pulse," in *Proc. IEEE Int. Conf. Comput. Commun. (ICCC)*, Oct. 2015, pp. 207–211.
[17] S. H. Yang, Y. F. Tang, X. K. Liu, and J. H. Liu, "Study on effects of high-altitude electromagnetic pulse to engine electronic control system," *Adv. Mater. Res.*, vols. 443–444, pp. 894–898, Jan. 2012.
[18] D. Zhou, M.-X. Wei, L.-H. Shi, and J. Cao, "Numerical simulation and experimental study of the impact of an early-time HEMP field on an engine speed acquisition system," *Int. J. Appl. Electromagn. Mech.*, vol. 61, no. 3, pp. 403–417, Nov. 2019.
[19] O. Aiello, P. Crovetti, and F. Fiori, "Investigation on the susceptibility of Hall-effect current sensors to EMI," in *Proc. 10th Int. Symp. Electromagn. Compat.*, Sep. 2011, pp. 368–372.
[20] Y. Tang, F. Zhu, and Y. Chen, "Analysis of EMI from pantograph-catenary arc on speed sensor based on the high-speed train model," *Appl. Comput. Electromagn. Soc.*, vol. 36, no. 2, pp. 205–212, Mar. 2021.
[21] Z. Qiao, A. Elhattab, X. Shu, and C. He, "A second-order stochastic resonance method enhanced by fractional-order derivative for mechanical fault detection," *Nonlinear Dyn.*, vol. 106, no. 1, pp. 707–723, Sep. 2021.
[22] Z. Sun and C. C. Chang, "Structural damage assessment based on wavelet packet transform," *J. Struct. Eng.*, vol. 128, no. 10, pp. 1354–1361, Oct. 2002.
[23] J. Yan, "Study on the electromagnetic compatibility of shaft end speed sensors in CRH3 electric multiple unit," M.S. thesis, Dept. Electr. Eng., Southwest Jiaotong Univ., Chengdu, China, 2015.
[24] N. Mora, B. Daout, M. Nyffeler, C. Romero, and F. Rachidi, "Revisiting the calculation of the early time HEMP conducted environment," *IEEE Trans. Electromagn. Compat.*, vol. 63, no. 1, pp. 111–124, Feb. 2021.
[25] *CST Microwave Studio, Version 2008*, Comput. Simul. Technol., Framingham, MA, USA, 2008.

HAITAO WANG was born in September 1978. He received the master's degree in mechanical engineering from the PLA University of Science and Technology. He is currently a Professor and the Director of the Army Engineering University of PLA, Nanjing, China, with a focus on equipment maintenance and management.

DONG ZHOU received the Doctorate degree from the School of Nanjing University of Aeronautics and Astronautics (NUAA), Nanjing, China, in October 2020. He is currently a Lecturer with the Army Engineering University of PLA, Nanjing, and devoted to the research on the coupling mechanism of engine strong electromagnetic pulse.

MINXIANG WEI received the Ph.D. degree in vehicle engineering from Xi'an Jiaotong University, Xi'an, China, in March 2001. He is currently a Professor in energy and power at the Nanjing University of Aeronautics and Astronautics. His research interests include vehicle electronics and automation, aviation piston engine electronic control, vehicle safety control, and electric vehicle control technology.

WEIWEI QIAN received the Ph.D. degree from the Nanjing University of Aeronautics and Astronautics, Nanjing, China, in 2020. He is currently with the School of Artificial Intelligence, Nanjing University of Information Sciences and Technology, Nanjing. His research interests include intelligent fault diagnosis and prognostics and transfer learning.